The Astrophysical Journal, 970:12 (12pp), 2024 July 20 https://doi.org/10.3847/1538-4357/ad49a0

Inferring Small Neutron Star Spins with Neutron Star–Black Hole Mergers

Ish Gupta
Institute for Gravitation and the Cosmos, Department of Physics, Pennsylvania State University, University Park, PA 16802, USA
Received 2024 February 12; revised 2024 May 1; accepted 2024 May 8; published 2024 July 11

Abstract

The precise measurement of neutron star (NS) spins can provide important insight into the formation and evolution of compact binaries containing NSs. While traditional methods of NS spin measurement rely on pulsar observations, gravitational-wave detections offer a complementary avenue. However, determining component spins with gravitational waves is hindered by the small dimensionless spins of the NSs and the degeneracy in the mass and spin parameters. This degeneracy can be addressed by the inclusion of higher-order modes in the waveform, which are important for systems with unequal masses. This study shows the suitability of NS–black hole mergers, which are naturally mass-asymmetric, for precise NS spin measurements. We explore the effects of the black hole masses and spins, higher-mode content, inclination angles, and detector sensitivity on the measurement of NS spin. We find that networks with next-generation observatories like the Cosmic Explorer and the Einstein Telescope can distinguish NS dimensionless spin of 0.04 (0.1) from zero at 1σ confidence for events within ∼350 (∼1000) Mpc. Networks with A+ and A$^\sharp$ detectors achieve similar distinction within ∼30 (∼70) Mpc and ∼50 (∼110) Mpc, respectively.

Unified Astronomy Thesaurus concepts: Gravitational waves (678); Neutron stars (1108); Compact objects (288); Pulsars (1306); Black holes (162); Astrophysical black holes (98)

1. Introduction

The current ground-based gravitational-wave (GW) detectors are sensitive to GWs from binaries containing black holes (BHs) and/or neutron stars (NSs). These compact objects form as the end products of the evolution of massive stars. The formation mechanism of such compact binaries can be broadly classified into two types—first, where two closely located massive stars evolve in isolation (Tutukov & Yungelson 1973; Postnov & Yungelson 2014), and second, where the binaries are formed due to dynamical interactions in dense stellar environments (Sigurdsson & Hernquist 1993; Benacquista & Downing 2013). The pathway followed for the binary formation and the processes it undergoes during its evolution leave their imprints on the system, particularly on the masses and spins of the components. Fortunately, by detecting the GWs from these systems, these parameters can be inferred, providing important insights into the formation and evolution of the binary (e.g., see Mastrogiovanni et al. 2022). As different formation channels lead to different parameters of the components (Abbott et al. 2016a; Gerosa & Berti 2017; Mandel & Farmer 2022), and a single formation channel cannot explain the properties of the detected binaries (Zevin et al. 2021), precise estimations of the mass and the spin distributions are pivotal for understanding the contributions of the various formation channels to the binary population.

The first direct detection of a GW was from a ∼65 $M_\odot$, nearly equal-mass, binary black hole (BBH) merger (Abbott et al. 2016b). This detection proved that BBHs can merge in Hubble time and allowed the determination of the merger rate for such binaries, rejecting pessimistic formation scenarios that predicted very low merger rate values (Belczynski et al. 2007; Mennekens & Vanbeveren 2014). While the components' masses were more than the expectations from low-mass X-ray binary systems (Farr et al. 2011), they were found to be consistent with both isolated and dynamical formation channels, provided that the corresponding metallicity was lower than solar metallicity (Abbott et al. 2016a; Belczynski et al. 2016). Since then, the Advanced Laser Interferometer Gravitational-Wave Observatory (aLIGO; Aasi et al. 2015; Abbott et al. 2018; Tse et al. 2019; Buikema et al. 2020) and the Advanced Virgo detector (Acernese et al. 2015, 2019) have detected ∼100 mergers by the end of the third observing run (Abbott et al. 2023a). Among these, the majority are BBH mergers, followed by two neutron star–black hole (NSBH)[1] mergers and two binary neutron star (BNS) mergers. Using the detected BBH mergers, significant constraints have been placed on the mass spectrum of BHs (Abbott et al. 2023b), revealing distinctive features that could contain information about the astrophysical processes at play (Zevin et al. 2017; Tiwari & Fairhurst 2021; Wong et al. 2021; Tiwari 2022; Farah et al. 2023). While the predictions for the masses of the components from different formation channels can overlap, the spin values and orientations can encode decisive information for distinguishing between the formation scenarios (Farr et al. 2017, 2018; Vitale et al. 2017). The isolated binary formation channels are, predominantly, expected to create slowly spinning binaries with spins aligned with the orbital angular momentum (Tutukov & YungelSon 1993; Belczynski et al. 2016; Zaldarriaga et al. 2018; Fuller & Ma 2019; Zevin & Bavera 2022; however, see also Kalogera 2000; O'Shaughnessy et al. 2017; Olejak & Belczynski 2021). On the other hand, binaries formed through dynamical exchanges are expected to have components with spins that are oriented isotropically (Rodriguez et al. 2016) and possibly with large magnitudes (Berti & Volonteri 2008). Unfortunately, as the

[1] In the literature, mergers with BHs and NSs are often referred to as NSBHs if the NS forms first and as BHNSs if the BH forms first. However, we use NSBH to refer to all mergers that contain an NS and a BH.

individual spins of the compact objects cannot yet be precisely measured using GW observations, the spin distribution of the BHs from the current observations remains uncertain (Vitale et al. 2022), leading to a lack of clarity about the dominant formation channel for the detected population.

The properties of the cosmic population of BNS and NSBH mergers are even more uncertain, owing to the limited number of GW observations. Currently, our expectations are informed by the Galactic pulsar observations, which point to a bimodal mass distribution, with the dominant peak at $\sim$1.4 $M_\odot$ and the minor peak at $\sim$1.8 $M_\odot$ (Antoniadis et al. 2016; Alsing et al. 2018; Farr & Chatziioannou 2020). NSs present in binaries are seen to coincide with the former peak (Ozel et al. 2012; Kiziltan et al. 2013). While GW170817 (Abbott et al. 2017a) seems to follow this trend as well, the component masses inferred for GW190425 (Abbott et al. 2020a) contradict it. Unlike the pulsar population, the NSs in BNS and NSBH mergers detected using GWs so far are consistent with a uniform distribution in mass (Landry & Read 2021; Abbott et al. 2023b).

Measuring the spin of an individual NS using GWs is trickier. This is due to the following two reasons. First, individual spins are difficult to measure. The GW signal for low-mass compact objects, like BNSs and NSBHs, is dominated by the inspiral—where the orbit of the binary shrinks due to the emission of GWs. This part of the signal is well approximated with the post-Newtonian (PN) formalism (Blanchet 2014), where the dominant spin effect appears at 1.5 PN order and is best represented by the effective spin parameter (Ajith et al. 2011):

$$\chi_{\rm eff} = \frac{m_1\chi_1 + m_2\chi_2}{m_1 + m_2} = \frac{\chi_1 + q\,\chi_2}{1+q}. \quad (1)$$

Here, (m_1, m_2) are the component masses, (χ_1, χ_2) are their dimensionless spin components aligned with the orbital angular momentum, and $q = m_2/m_1 \leqslant 1$ is the mass ratio. Further, the contribution to the GW phase for nonprecessing systems to leading order in spin can be written as

$$\Psi(f) = \frac{3}{128(\pi f\mathcal{M})^{5/3}}\Bigg[1 + \nu^2\left(\frac{3715}{756} + \frac{55\eta}{9}\right) + \nu^3\left(\frac{113}{3}\chi_{\rm eff} - \frac{76\eta}{3}\chi_s - 16\pi\right)\Bigg], \quad (2)$$

where $\mathcal{M} = M\eta^{3/5}$ is the chirp mass, $\eta = q/(1+q)^2$ is the symmetric mass ratio, $\nu = (\pi f M)^{1/3}$ is the PN expansion parameter, $M = m_1 + m_2$ is the total mass, f is the frequency of the quadrupolar part, and $(\chi_s = \chi_1 + \chi_2)/2$. The dominant effect of spins on the phase can be encapsulated in a reduced spin parameter, $\chi_{\rm PN}$, defined as

$$\chi_{\rm PN} = \chi_{\rm eff} - (76\eta/113)\chi_s. \quad (3)$$

As the lowest-order contribution to the phase depends on the chirp mass $\mathcal{M}$, it is well measured. Now, looking specifically at the ν^2 (1 PN) and the ν^3 (1.5 PN) terms (Baird et al. 2013),

$$\Delta\Psi(f) = \frac{3\nu^2}{128(\pi f\mathcal{M})^{5/3}}\left[\frac{3715}{756} + \frac{55\eta}{9} + \nu\left(\frac{113}{3}\chi_{\rm PN} - 16\pi\right)\right], \quad (4)$$

we see that η, or equivalently the q, can be varied without varying $\mathcal{M}$ to mimic the effect of spin (although it will also have to account for the changing ν with frequency) at this order. This, together with the dependence of $\chi_{\rm eff}$ on q, represents the degeneracy between mass and spin parameters, which hampers the measurement of the individual spins (Cutler & Flanagan 1994; Baird et al. 2013).

Second, the dimensionless spins of NSs are expected to be small by the time of merger. Pulsar observations suggest that NSs can be rapidly rotating. While most of the cataloged pulsars have periods $P \sim 0.5$ s, a significant and distinct fraction, called millisecond pulsars, can have periods $P \lesssim 30$ ms (Lorimer 2008). The fastest-rotating known pulsar, PSR J1748-2446ad, has a period of $P \sim 1.4$ ms, translating to a dimensionless spin $\chi \leqslant 0.4$ (Hessels et al. 2006; Abbott et al. 2017a). The fastest-spinning NS that is part of a BNS that will merge within Hubble time is PSR J0737-3039, with a period of 22 ms (Burgay et al. 2003). While this is still rapid, pulsar rotation is expected to slow down with time. This is because pulsars accelerate charged particles that, in turn, emit radiation, and this radiation carries away the rotational kinetic energy. In fact, PSR J0737-3039 is expected to spin down to $\chi \lesssim 0.04$ at merger (Abbott et al. 2017a). As ground-based GW observatories are only expected to detect these binaries close to merger, the NS dimensionless spins are expected to be $\lesssim 0.04$.

Fortunately, the mass–spin degeneracy can be broken with the inclusion of higher-order modes and precession (Chatziioannou et al. 2014) in the waveform. While the quadrupolar (2, 2) mode dominates the GW from nonprecessing, equal-mass, and face-on (inclination angle $\iota = 0°$) systems, the subdominant higher-order modes get activated for systems with unequal masses (Pan et al. 2011; Roy et al. 2021; and for precessing systems). We expect the contribution of these higher modes (HMs) to increase with the asymmetry in the masses. As the NS mass function is restricted to a small range of values (Margalit & Metzger 2017; Shibata et al. 2017, 2019; Rezzolla et al. 2018; Ruiz et al. 2018; Suwa et al. 2018; Abbott et al. 2020b; Doroshenko et al. 2022), we do not expect a significant contribution of HMs in the inspiral of BNS mergers. On the other hand, NSBH mergers will have unequal masses. Population synthesis studies (like Broekgaarden et al. 2021) that have looked at NSBH mergers formed through isolated binary formation channels find that the BH mass in NSBH mergers rarely exceeds 20 $M_\odot$, with the peak of the mass function lying between 5 $M_\odot$ and 15 $M_\odot$. This is also supported by the inference of the BH mass spectrum from detected NSBH mergers (Biscoveanu et al. 2022). Given that the expected NS masses are less than 2 $M_\odot$, NSBH systems will be largely asymmetric, with $q \lesssim 0.4$. Thus, due to the contribution of HMs to the GW signal, NSBH systems can be instrumental in measuring the NS spin ($\chi_{\rm NS}$).

In this work, we assess the precision with which $\chi_{\rm NS}$ can be measured from nonprecessing NSBH mergers. The "nonprecessing" choice is partly motivated by our focus on binaries formed through isolated binary formation channels (see Section 2.2) and partly due to computational feasibility (briefly discussed in Section 3). We find that the precision in the measurement of $\chi_{\rm NS}$ strongly depends on the BH spin ($\chi_{\rm BH}$), with high BH spins ($\chi_{\rm BH} \geqslant 0.6$) being conducive to more precise $\chi_{\rm NS}$ measurement. We also show the importance of HMs in improving the measurement precision, by comparing

the bounds placed on $\chi_{\rm NS}$ using a waveform model that only contains the quadrupolar mode with one that also contains HMs, at varying inclination angles. As the detected NSBH events fail to constrain $\chi_{\rm NS}$ (Abbott et al. 2021, 2023a, 2023b), we focus on the abilities of next-generation (XG) GW observatories in measuring the same. We find that a five-detector A+ (Miller et al. 2015; Abbott et al. 2018) (three-detector A$^\sharp$) (Fritschel et al. 2022) network might distinguish $\chi_{\rm NS} = 0.04$ from zero at 1σ confidence for an NSBH merger at $\sim$30 ($\sim$50) Mpc, while a network with the Einstein Telescope (ET; Punturo et al. 2010; Hild et al. 2011; Branchesi et al. 2023) and two Cosmic Explorers (CEs; Abbott et al. 2017b; Reitze et al. 2019; Evans et al. 2021; Gupta et al. 2023b; Evans et al. 2023) can accomplish the same for an NSBH merger at $\sim$350 Mpc. Based on these results, we claim that *if* there exists a subpopulation of NSBH binaries in nature that merge within Hubble time and contain rapidly spinning NSs, then XG observatories will discern such NSs from slowly or nonspinning ones, identifying extragalactic NSs with millisecond rotational periods without electromagnetic observations.

In this study, we emphasize the significance of measuring the NS spin with high precision. However, it is also vital to highlight that breaking the mass–spin degeneracy also enhances BH spin measurements (see Section 4.1). This improvement holds astrophysical significance, since accurately determining $\chi_{\rm BH}$ can provide valuable insights into the formation processes underlying binary creation. For a brief discussion of this aspect, refer to Section 2.2.

The rest of the paper is structured as follows. In Section 2, we build on the motivation for this study. The description of the employed parameter estimation techniques, the NSBH systems that are considered, and the GW network configurations that are used are presented in Section 3. In Section 4, we show the constraints on $\chi_{\rm NS}$ that can be placed with NSBH mergers, accompanied by an analysis of how BH parameters, the presence of HMs, and detector sensitivity can affect the precision with which $\chi_{\rm NS}$ can be estimated. Our conclusions are summarized in Section 5.

2. Motivation

In this section, we describe the motivation for considering NSBH mergers to precisely measure the NS spin. In Section 2.1, we use PN expressions to show the utility of HMs in improving the measurement of $\chi_{\rm NS}$. In Section 2.2, we discuss the astrophysical processes that can lead to the formation of NSBH systems with rapidly spinning NSs that merge within Hubble time.

2.1. Theoretical Arguments

In Section 1, we explained the degeneracy between the mass and spin parameters using the PN expansion of the GW phase to leading order in spin. We encapsulated the effect of spin on the phase at this order in the term $\chi_{\rm PN}$, which is a function of $\chi_{\rm eff}$ and χ_s. For BNS systems, the mass ratio is close to 1, leading to $\chi_{\rm eff} \sim \chi_s$. Thus, while these combinations of component spins can be measured to significant precision, it is difficult to disentangle the values of individual spins from them. These degeneracies could be affected due to higher-order spin effects, including the effect of spin-induced quadrupole moments on the phase (Krishnendu et al. 2017; Nagar et al. 2018; Dietrich et al. 2019). However, given that the values of $\chi_{\rm NS}$ are expected to be small, we do not expect these effects to drastically improve the measurement of NS spins.

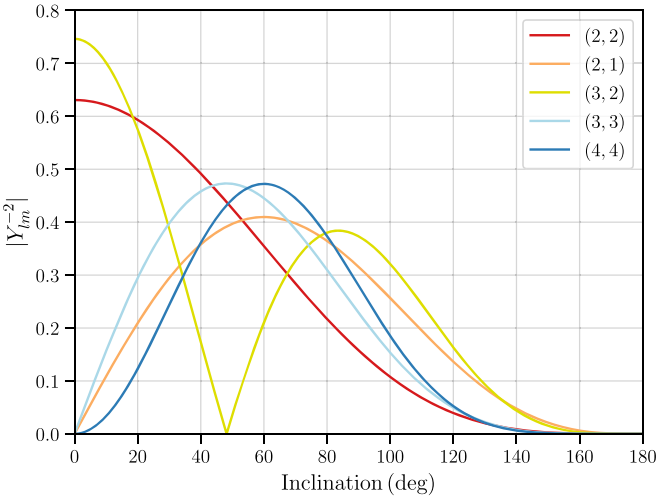

Figure 1. The variation of the absolute value of Y^{-2}_{lm} with the inclination angle for different HMs. $|Y^{-2}_{l-m}|$ are the same as $|Y^{-2}_{lm}|$, but mirrored about 90°.

For NSBH systems, we expect $\chi_{\rm NS}$ to be small and the mass ratio to be much smaller than 1. With these assumptions,

$$\chi_{\rm eff} = \frac{\chi_{\rm BH} + q\,\chi_{\rm NS}}{1+q} \approx \chi_{\rm BH},$$

i.e., most of the information contained in $\chi_{\rm eff}$ is about $\chi_{\rm BH}$, as the contribution of $\chi_{\rm NS}$ is weighed down by q. While $\chi_{\rm BH}$ and $\chi_{\rm NS}$ are at equal footing in χ_s, the contribution of χ_s compared to $\chi_{\rm eff}$ is weighed down by η (as, by definition, $\eta \leqslant 1/4$).

The HMs also contain contributions from the spins, which can help improve the measurements of individual spins of binary components. The complex time-domain GW strain $h(t)$ can be decomposed in the basis of -2 spin-weighted spherical harmonics Y^{lm}_{-2},

$$h(t, \boldsymbol{\lambda}) = \sum_{l=2}^{\infty} \sum_{m=-l}^{l} Y^{lm}_{-2}(\iota) h_{lm}(t, \boldsymbol{\lambda}), \tag{5}$$

where ι is the inclination angle and $\boldsymbol{\lambda}$ is the set of parameters, including the masses and spins of the binary components, affecting the strain. For nonprecessing systems, the $(l, \pm m)$ modes obey the symmetry $h_{lm} = (-1)^l\, \bar{h}_{l-m}$. The phase of the (l,m) modes has an approximate relation to the phase of the (2, 2) mode in the inspiral regime, given by $\Phi_{lm} \approx \frac{m}{2}\Phi_{22}$, which also means that the frequency corresponding to the $(l, \pm m)$ mode is $m/2$ times the frequency of the $(2, \pm 2)$ mode. On the other hand, the amplitudes of the HMs contain important differences. First, the relative contribution of the (l,m) mode to the signal depends on the inclination angle, which enters the equation through Y^{-2}_{lm}. Figure 1 shows the dependence of the absolute value of Y^{-2}_{lm} with inclination for different modes. Second, various combinations of component spins contribute to the amplitude of the (2, 2) mode and the HMs. The leading-order spin contributions to h_{lm} are listed in Table 1, with lower-order terms only depending on mass parameters. Based on Table 1 and Figure 1, we conclude the following:

Table 1
The Leading-order Spin Terms That Contribute to the Amplitudes of Some of the Different (l,m) Modes, Retrieved from Pan et al. (2011)

Mode	PN	PN (χ)	Leading-order Spin Terms
(2, 1)	0.5	1	$\frac{4i}{R}\sqrt{\frac{\pi}{5}}\ \eta M\ \tilde{\chi}$
(2, 2)	0	1.5	$\frac{32}{3R}\sqrt{\frac{\pi}{5}}\ \eta M(\chi_{\rm eff}-\eta\chi_s)$
(3, 2)	1	1.5	$\frac{32}{3R}\sqrt{\frac{\pi}{7}}\ \eta^2 M\ \chi_s$
(3, 3)	0.5	2	$\frac{3i}{2R}\sqrt{\frac{6\pi}{7}}\ \eta M((4-5\eta)\tilde{\chi}-14\eta\chi_a)$
(4, 4)	1	2.5	$\frac{256}{9R}\sqrt{\frac{\pi}{7}}\ \eta M\left[(-\frac{2}{3}+\frac{13}{5}\eta)\chi_{\rm eff}+\frac{2\eta}{5}\left(\frac{1}{3}-7\eta\right)\chi_s\right]$

Note. Here, the column titled "PN" lists the PN order of the leading-order term that contributes to the amplitude of the mode, and the "PN (χ)" column lists the leading order at which the spin terms show up in the amplitudes of the respective modes. Similar to $\chi_{\rm eff}$, we introduce another combination of component spins and mass ratio $\tilde{\chi}=\frac{\chi_{\rm BH}-q\,\chi_{\rm NS}}{1+q}$, which contains the leading-order spin effects on the (2, 1) and the (3, 3) mode amplitudes. We have also used the asymmetric spin combination, $\chi_{\rm a}=(\chi_{\rm BH}-\chi_{\rm NS})/2$.

1. The leading-order term in the (2, 2) mode amplitude is at 0 PN. This makes (2, 2) the dominant mode in the GW strain.
2. Only the (2, 2) and (3, 2) modes contribute to the signal for face-on ($\iota=0°$) systems. The (2, 1), (3, 3), and (4, 4) modes peak at $\iota>40°$.
3. The (2, 2), (3, 2), and (4, 4) modes contain positive combinations of spins, like $\chi_{\rm eff}$ and χ_s, whereas the (2, 1) and (3, 3) modes contain negative combinations, like $\tilde{\chi}$ and χ_a.
4. In their respective modes, the χ_s (χ_a) spin terms are suppressed by a factor of η compared to the $\chi_{\rm eff}$ ($\tilde{\chi}$) term.

The different ways in which the mass and spin terms interact in the various (l,m) modes help remove the degeneracy between these parameters. While $\chi_{\rm eff}$ and $\tilde{\chi}$ values for BNS systems are expected to be small, they can be significant for NSBH systems if the BH is highly spinning. Larger values of $\chi_{\rm eff}$ and $\tilde{\chi}$ result in longer inspirals and greater imprints of spins on the amplitude and phase of the GW, improving their measurability. Thus, we expect a correlation between greater $\chi_{\rm BH}$ values and better measurement of $\chi_{\rm NS}$. This expectation will be validated in Section 4.1.

To better illustrate the effect of the HMs, we calculate the Fisher matrix element ($\Gamma_{\chi_{\rm NS}}$) for a typical NSBH system using `gwbench` (Borhanian 2021). $\Gamma_{\chi_{\rm NS}}$ is a measure of the amount of information about $\chi_{\rm NS}$ that can be extracted from the GW strain. For demonstration, we choose the *plus* polarization of the strain and calculate

$$h^{+}_{lm,\chi_{\rm NS}}(f)=\frac{\partial h^{+}_{lm}(f)}{\partial\chi_{\rm NS}}, \tag{6}$$

$$\gamma^{+}_{\chi_{\rm NS}}(f)=\frac{h^{+}_{lm,\chi_{\rm NS}}(f)\bar{h}^{+}_{lm,\chi_{\rm NS}}(f)}{S_n(f)}, \tag{7}$$

$$\Gamma^{+}_{\chi_{\rm NS}}=4\Re\int_{f_{\rm low}}^{f_{\rm high}}\gamma^{+}_{\chi_{\rm NS}}(f)df, \tag{8}$$

where $h^{+}_{lm}(f)$ is the *plus* polarization of the (l,m) mode in the frequency domain obtained using IMRPhenomXHM (García-Quirós et al. 2020) for an NSBH system with a 10 $M_\odot$ BH and a 1.4 $M_\odot$ NS, with the power spectral density (PSD; S_n) associated with the 40 km CE detector considered between $f_{\rm low}=5$ Hz and $f_{\rm high}=2048$ Hz (see Appendix A for more information). We choose $\chi_{\rm BH}=0.4$ and $\chi_{\rm NS}=0.04$. Note that the square root of the inverse of the full Fisher matrix gives the measurement errors on the parameters. However, due to the process of inversion, the measurement precision on $\chi_{\rm NS}$ is not determined just from $(\Gamma^{+}_{\chi_{\rm NS}})^{-1/2}$, but has contributions from the correlations between $\chi_{\rm NS}$ and all the other GW parameters.

Hence, keeping in mind that $(\Gamma^{+}_{\chi_{\rm NS}})^{1/2}$ is only an indicator of the contribution of different modes, we show how these contributions vary with the inclination angle and the frequency in Figure 2. The left panel shows the contributions of the different (l,m) modes to the measurement of $\chi_{\rm NS}$. The effect of the variation of $|Y^{-2}_{lm}|$ (see Figure 1) with inclination is apparent. As expected, the bulk of the information about $\chi_{\rm NS}$ comes from the (2, $\pm$2) mode across the various inclination angles. The second-strongest contribution comes from the (3, $\pm$3) mode, which considerably informs the $\chi_{\rm NS}$ estimates for systems with $\iota>20°$. At high inclination angles, the contribution from the (3, $\pm$3) mode can reach about one-third the contribution of the (2, $\pm$2) mode (see Mills & Fairhurst 2021 for details of the importance of different modes). In the right panel, we show $\gamma^{+}_{\chi_{\rm NS}}(f)$ as a function of frequency, but normalized by its integral over the frequency band $\Gamma^{+}_{\chi_{\rm NS}}$. The normalization removes information about the relative importance of each mode, which is already shown in the left panel, and allows the portrayal of frequency regions in which each of the modes dominates. The (2, $\pm$2) and (2, $\pm$1) modes contribute predominantly to the lower frequencies, whereas the other HMs contribute to the higher frequencies as well. The information from the waveform that contains the (2, $\pm$2) and the HMs, shown in black, follows the (2, $\pm$2) mode curve, with oscillations due to the constructive and destructive interference between the (2, $\pm$2) mode and the HMs (Arun et al. 2009).

It is important to note that the choice of $S_n(f)$ affects the frequency regions to which the different modes contribute the most. The PSD corresponding to CE 40 km is relatively flat at lower frequencies, where the systems spend the majority of their inspiral. However, aLIGO has poor low-frequency sensitivity (see Figure 7), which will result in the shift of the curves shown in the right panel of Figure 2 toward higher-frequency values. This shift has been specifically shown for the (2, $\pm$2) mode with aLIGO sensitivity in Figure 2.

From the theoretical considerations involving the PN theory and Fisher estimates, we conclude that the (2, 2) mode will dominate the $\chi_{\rm NS}$ measurement, followed closely by the (3, 3) mode, especially for near edge-on ($\iota=90°$) systems. We highlight that η combines differently with different spin contributions in the amplitude of the HMs. We also posit that a large $\chi_{\rm BH}$ value will be conducive to $\chi_{\rm NS}$ measurement.

2.2. Astrophysical Considerations

As discussed in Section 1, pulsar observations have shown that rapidly rotating NSs can exist in binary configurations that merge within Hubble time. Further, in Section 2.1, we assert that for an NSBH system, larger values of BH spin will correspond to better measurements of the NS spin. In this section, we assess the formation scenarios for NSBH systems,

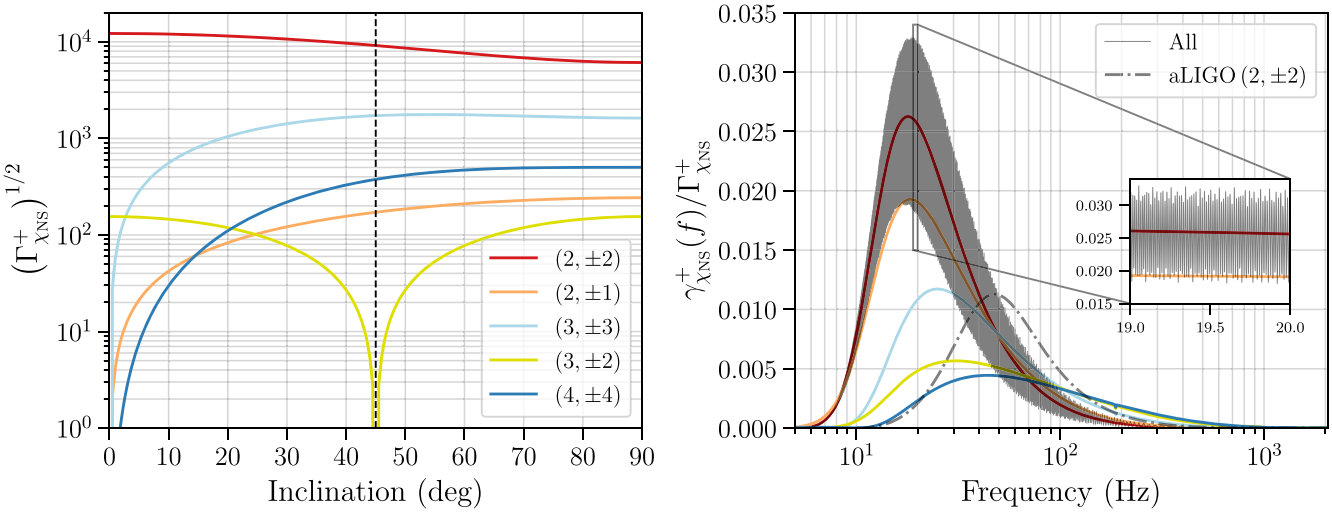

Figure 2. Left: the square root of the Fisher term corresponding to $\chi_{\rm NS}$ for the various (l,m) modes as a function of inclination angle (see Equations (6)–(8) for definitions of the various terms). The dotted vertical line indicates $\iota = 45°$. Right: assuming $\iota = 45°$, the figure shows the normalized Fisher term as a function of frequency for the different (l,m) modes separately, whereas the black curve shows the normalized Fisher term for the full waveform that contains all the modes. The highly oscillatory nature of the full waveform, due to constructive and destructive interference between modes, is highlighted in the inset. The 40 km CE PSD was used for obtaining the Fisher estimates. Using a different PSD, such as that for aLIGO, which has worse sensitivity at lower frequencies, will shift the curves toward higher frequencies, which is shown for the (2, ±2) mode with the dotted–dashed line.

via isolated binary formation channels, with a rapidly rotating NS and, preferably, a highly spinning BH.

One way NSs can attain their spins is due to the collapse of an initially spinning Chandrasekhar core. However, as the mass transfer from the core to the outer layers before collapse is expected to be highly efficient (Cantiello et al. 2014), the cores right before collapse are likely to be slowly spinning, leading to slowly spinning compact stars post-collapse (Fuller & Ma 2019). Recent studies (Coleman & Burrows 2022; Burrows et al. 2023b) suggest another method to spin up the NS at birth—through the stochastic accretion of infalling matter after the core-collapse supernova explosion. In fact, Burrows et al. (2023b) find that NSs created in this way from lower-mass ($<10\ M_{\odot}$) zero-age main-sequence (ZAMS) stars have lower spins ($P \sim \mathcal{O}(10^3)$ ms) and natal kick velocities ($v_{\rm kick} \lesssim 200\,{\rm km\,s^{-1}}$), whereas those from higher-mass ($>10\ M_{\odot}$) ZAMS stars generally have higher spins ($P \sim \mathcal{O}(10)$ ms) and natal kick velocities ($v_{\rm kick} \gtrsim 400\,{\rm km\,s^{-1}}$). While the latter are favorable for generating rapidly spinning NSs, the high kick velocities could disrupt the binary system, reducing the chance of such an NS existing in binary configurations. A similar trend is seen in BHs, where BHs formed after core collapse are seen to have large spins and kicks, whereas those born from failed explosions have smaller values for spins and kicks (Burrows et al. 2023a, 2023b).

Stars present in binary configurations can undergo other physical processes that can lead to rapidly rotating compact objects. The primary, more massive, star is the first to evolve off the main sequence and undergo a supernova explosion to become a compact object. Assuming the binary survives this explosion, the second star evolves off the main sequence, expands, and initiates the common envelope phase (Soberman et al. 1997; Ge et al. 2010, 2015; Vigna-Gómez et al. 2018). The common envelope extracts energy from the binary and, if ejected successfully, leaves behind a tighter binary with smaller period, containing a compact object and a Wolf–Rayet star (for other scenarios, see Broekgaarden et al. 2021 and references therein). In certain cases, the Wolf–Rayet star can expand farther and fill its Roche Lobe, leading to stable mass transfer from this helium star to the compact object (Delgado & Thomas 1981; Tauris et al. 2015). This mass-transfer episode can spin up the firstborn compact object (Thorne 1974; Tauris et al. 2015). If the BH is formed first, Wang et al. (2024) show that super-Eddington accretion can result in a highly spun-up ($\chi_{\rm BH} > 0.6$) BH. If the NS is formed first, its spin can be further increased (often referred to as recycling the NS/pulsar), leading to more massive NSs with millisecond periods (Ozel et al. 2012) and the possible burial of their magnetic fields (Zhang & Kojima 2006; Chattopadhyay et al. 2021). As the spindown rate of the NS increases with the magnetic field strength and decreases with mass, these recycled NSs can have considerable spins at the time of merger. In their simulation study, Chattopadhyay et al. (2021) find that ∼20% of the NSBH systems where the NS is formed first contain a pulsar and more than 96% of such *radio-alive* systems are noted to be recycled. They also find that for a significant fraction of such binaries, $\chi_{\rm NS} > 0.05$ during merger. However, only ∼3% of the NSBH systems in their simulations, which are expected to be detected by the LIGO–Virgo detectors, contain a firstborn NS. For the rest of the systems, the NS is born second and cannot get spun up due to accretion. Other studies also estimate the rate of NSBH mergers with firstborn NSs to be subdominant to those with second-born NSs, with the ratio of rates for the former to those of the latter ranging from $\mathcal{O}(0.001) - \mathcal{O}(0.1)$ (Broekgaarden et al. 2021; Chattopadhyay et al. 2022).

The helium core of the secondary, present in a close binary, can also get spun up due to tidal locking (Kushnir et al. 2017; Qin et al. 2018; Fuller & Ma 2019; Bavera et al. 2021). Fuller & Ma (2019) find that the spin of second-born BHs can exceed the value of 0.5 for such systems. However, as the tidal torques depend on the orbital angular frequency, the binary has to be very close ($P_{\rm orb} \lesssim 1$ day; Fuller & Lu 2022) for tidal locking to take effect. Fuller & Lu (2022) find that for the orbital period $P_{\rm orb} = 0.5$ day, second-born NSs can be spun up to millisecond periods. As shorter orbital separations are required for tidal synchronization, the companion has to be small enough to fit in the orbit. Compact objects like NSs and BHs make ideal companions that can tidally spin up the helium core, which is why it is the secondary that is expected to spin up appreciably

due to tidal locking (Hu et al. 2023; Wang et al. 2024). Using Qin et al. (2018), Chattopadhyay et al. (2021) find that a significant fraction of the second-born BHs in NSBH systems can have spins greater than 0.4. They also probe the effect of metallicity on the NS spins in NSBH mergers, finding that lower metallicity results in lower mass loss through stellar winds. This results in more massive helium stars, which expand less and result in lower mass transfer. Thus, the NSs are not efficiently recycled due to the accretion for such systems.

While the problem of binary formation and evolution is dominated by modeling uncertainties, several plausible pathways lead to the formation of NSBH binaries with rapidly rotating components, even under the constraints of the isolated binary formation mechanisms. Although the actual merger rates and properties of such systems can only be ascertained with more observations, it is worth investigating if these properties can be precisely determined with future GW observatories. Given the specific and countable scenarios that lead to the presence of a rapidly rotating NS during merger, decisively differentiating the spin of the NS from 0 can illuminate the astrophysical processes that contribute to cosmic binary formation and evolution, and the physics that affects the spindown of NSs. This is the objective of this work, and the particular question of the precision of the NS spin measurement will be answered in Section 4.

3. Methodology

To explore the precision with which $\chi_{\rm NS}$ can be measured using NSBH mergers, we apply Bayesian parameter estimation on simulated GW data. The GW data d is the detector response defined by

$$d(t, \boldsymbol{\theta}) = n(t) + s(t, \boldsymbol{\theta}), \tag{9}$$

where $n(t)$ is the noise and $s(t, \boldsymbol{\theta})$ is the GW signal, which depends on a set of intrinsic and extrinsic parameters (including masses and spins), $\boldsymbol{\theta}$. Then, the posterior distribution $p(\boldsymbol{\theta}|d)$ can be obtained using

$$p(\boldsymbol{\theta}|d) = \frac{p(d|\boldsymbol{\theta})p(\boldsymbol{\theta})}{\mathcal{Z}}. \tag{10}$$

Here, $p(d|\boldsymbol{\theta})$ is the likelihood function, $p(\boldsymbol{\theta})$ is the prior on the GW parameters, and $\mathcal{Z} = \int p(d|\boldsymbol{\theta})p(\boldsymbol{\theta})d\boldsymbol{\theta}$ is the evidence. The probability distribution for $\chi_{\rm NS}$ can be retrieved from the joint posterior distribution by marginalizing it over all other parameters (Thrane & Talbot 2019):

$$p(\chi_{\rm NS}|d) = \int \left(\prod_{\theta_i \neq \chi_{\rm NS}} d\theta_i \right) p(\boldsymbol{\theta}|d). \tag{11}$$

The calculation of these posterior distributions is a computationally challenging task and is accomplished using stochastic samplers (Metropolis et al. 1953; Hastings 1970; Skilling 2004). However, covering the prior space and sufficiently mapping the likelihood surface could involve $\mathcal{O}(10^8)$ likelihood evaluation, which can be time-consuming. This is especially true for the long and high-signal-to-noise-ratio (S/N) signals expected to be detected by XG observatories. Hence, several likelihood evaluation and sampling techniques have been introduced to speed up this process (Canizares et al. 2015; Pankow et al. 2015; Smith et al. 2016, 2020; Vinciguerra et al. 2017; Talbot et al. 2019; Green et al. 2020; Morisaki & Raymond 2020; Morisaki 2021; Williams et al. 2021; Edwards et al. 2023; Morisaki et al. 2023; Pathak et al. 2023, 2024; Tiwari et al. 2023; Wong et al. 2023).

For accelerated parameter estimation, we use the relative binning technique (Cornish 2010, 2021; Zackay et al. 2018) implemented in Bilby (Ashton et al. 2019; Romero-Shaw et al. 2020; Krishna et al. 2023). The relative binning technique relies on the assumption that the ratio of the waveform between neighboring points in the parameter space varies smoothly. The waveform corresponding to the maximum likelihood point in the parameter space is chosen as the fiducial waveform, and the waveforms around this point are obtained using piecewise linear functions informed by this fiducial waveform. These approximations can amount to speed ups by $\mathcal{O}(10^3)$, without compromising significantly on the accuracy (Zackay et al. 2018; Krishna et al. 2023). However, waveforms that contain contributions of HMs and involve precession can be highly oscillatory and may not be well approximated by piecewise linear functions. While Krishna et al. (2023) show that the technique fares well even for asymmetric systems, a mode-by-mode adaptation of relative binning has also been proposed (Leslie et al. 2021), which approximates each (l,m) mode separately and then adds them together to obtain the full (approximated) waveform. As our study only considers NSBH systems whose spins are aligned with the orbital angular momentum, we use the original relative binning technique and its implementation in Bilby (Krishna et al. 2023), but also validate our results against those obtained with our implementation of the mode-by-mode technique, and find them to be consistent.

The GW signals are generated using the IMRPhenomXHM waveform (García-Quirós et al. 2020), which is an aligned-spin frequency-domain waveform that includes the (2, 2), (2, 1), (3, 3), (3, 2), and (4, 4) modes. We set the R.A. $\alpha = 78.^{\circ}78$, decl. $\delta = -69.^{\circ}37$, phase $\phi_c = 74.^{\circ}48$, polarization angle $\psi = 152.^{\circ}34$, and the geocentric time $t_c = 1126259642.413$ s. Other than Section 4.3, where we look at various detector sensitivities, we inject GW signals in a network of one ET and two CEs (one with 40 km arms and the other with 20 km arms), henceforth referred to as the ECC network. Our simulated binaries comprise NSBH systems with a 10 $M_\odot$ BH and a 1.4 $M_\odot$ NS (henceforth, referred to as a 10+1.4 system), at $\iota = 45^{\circ}$. We assess the effect of varying BH mass in Section 4.1 and ι in Section 4.2. The BH spins can range from [0,0.8], whereas the NS spins are only considered up to 0.1 (an informed upper bound based on the results of Chattopadhyay et al. 2021).

For all the simulations, we use uniform priors in χ_1 and χ_2 (i.e., $\chi_{\rm BH}$ and $\chi_{\rm NS}$, respectively) bounded between $[-0.99,0.99]$ and uniform priors in component masses. For all other parameters, we choose the default Bilby priors. We predominantly use the `nessai` (Williams 2021; Williams et al. 2021, 2023) and `pymultinest` (Buchner et al. 2014) samplers for our runs, and perform spot checks with the `dynesty` (Speagle 2020; Koposov et al. 2023) sampler to ensure consistency.

Note that an NS may get tidally disrupted by the BH before the merger (Kyutoku et al. 2021). These tidal effects will affect the waveform and can potentially contribute to $\chi_{\rm NS}$ constraints due to spin-induced quadrupole moments. These effects are not considered in IMRPhenomXHM, as it is predominantly used for BBH systems. While high BH spins favor the disruption of the NS, a low mass ratio (i.e., a heavy BH) will disfavor it. We

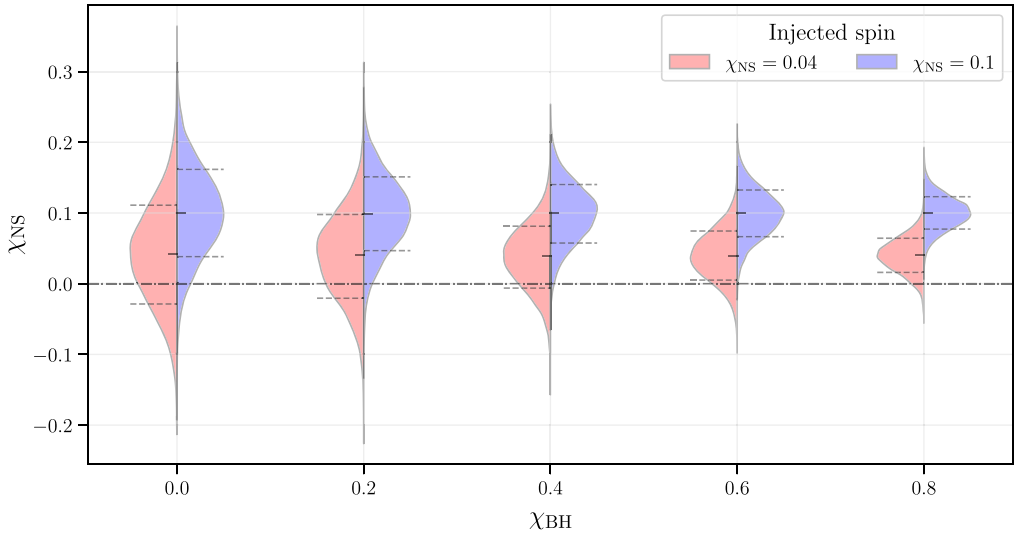

Figure 3. The posterior distributions for χ_{NS} as a function of χ_{BH}. The red and blue plots show the posteriors for systems where χ_{NS} is set to 0.04 and 0.1, respectively. Along with the posteriors, we also show the median (small solid horizontal line) and the boundaries of the $1-\sigma$ region (dashed horizontal lines). The posteriors correspond to a system with a BH of mass 10 $M_\odot$ and an NS of mass 1.4 $M_\odot$ at an inclination angle of 45°. The dashed–dotted horizontal line indicates $\chi_{NS} = 0$.

explore the effect of the tidal deformability of the NS on χ_{NS} measurement in Appendix B.

In this work, we have not considered several issues that will affect parameter estimation with XG observatories. Networks with the ET and CEs are expected to detect the majority of compact binary mergers that will occur in the Universe (Branchesi et al. 2023; Gupta et al. 2023b). Due to the abundance of mergers, several signals are expected to overlap at any instance, leading to confusion noise that may affect the detectability of individual events (Wu & Nitz 2023) and bias the parameter inference (Samajdar et al. 2021). For a fraction of these signals that will be detected with high S/Ns, the systematic errors due to the limited accuracy of the currently used waveforms will dominate the statistical errors in parameter measurement, resulting in a biased estimation of binary properties (Pürrer & Haster 2020; Hu & Veitch 2022). These systematic biases increase with χ_{BH} (Dhani et al. 2024), which is especially relevant to this work. Another contributing hurdle is the systematic error due to detector calibration, which can lead to significant uncertainty in amplitude and phase between 20 and 2000 Hz (Sun et al. 2020, 2021). Such calibration errors can result in biased parameter, and cosmological, inference (Huang et al. 2022). We do not account for these effects, in the hope that these challenges will be mitigated before XG observatories are operational (e.g., see Janquart et al. 2023; Johnson et al. 2024).

4. Results

In this section, we show the results of the parameter estimation runs performed on simulated NSBH GW events. Focusing on the precision with which χ_{NS} can be measured, we assess the impacts of BH mass and spin as well as those of ι and HMs on these measurements in Sections 4.1 and 4.2, respectively. Note that for a system situated at a particular luminosity distance D_L, changing the masses/spins of the compact objects or the inclination angle will affect the S/N associated with the detected signal, which has direct consequences for the bounds that can be placed on χ_{NS}. To isolate the effects of binary parameters from the effect of the S/N, all the systems considered in Sections 4.1 and 4.2 have the same S/N (∼700), which is achieved by varying D_L appropriately. The effects of detector sensitivity and luminosity distance (and, consequently, the S/N) are discussed in Section 4.3.

4.1. Effects of BH Mass and BH Spin

In Section 2.1, we claimed that a high value of χ_{BH} should improve the χ_{NS} measurement. To validate this, we consider $10+1.4$ NSBH systems at $\iota = 45°$ and varying (χ_{BH}, χ_{NS}) values, and report the 68% confidence interval (i.e., 1σ) on the inferred values of χ_{NS} in Figure 3. It is evident that the bounds on χ_{NS} improve with higher χ_{BH} values, which validates our expectations. For the chosen S/N (corresponding to systems located at $D_L \in (200, 205)$ Mpc), a highly spinning NS with $\chi_{NS} = 0.1$ can be easily differentiated from a nonspinning one, even for a nonspinning BH companion. A slightly slower NS with $\chi_{NS} = 0.04$ can only be differentiated from 0 with 1σ confidence at this S/N if $\chi_{BH} > 0.4$. As the χ_{NS} values are small, the bounds are not significantly affected by the true value of the NS spin.

The effect of the mass of the BH (m_{BH}) needs greater care. Keeping the S/N constant, as m_{BH} increases, so does the contribution of the HMs to the signal (Mills & Fairhurst 2021), which should be favorable for spin measurements. However, this also leads to a lower value for q (and η), which reduces the contribution of χ_{NS} to χ_{eff} and $\tilde{\chi}$ and those of χ_s and χ_a to the amplitude of the modes (see Table 1). To evaluate the effect of m_{BH}, we fix the mass and spin of the NS to 1.4 $M_\odot$ and 0.04, respectively, and perform parameter estimation for systems with $m_{BH} \in \{5\ M_\odot,\ 10\ M_\odot,\ 15\ M_\odot,\ 20\ M_\odot\}$ and $\chi_{BH} \in \{0.2,\ 0.4,\ 0.6,\ 0.8\}$. For this set of 16 events, we state the half-width of the 68% confidence interval of the bounds on χ_{NS} and χ_{BH} (referred to as $\Delta\chi_{NS}$ and $\Delta\chi_{BH}$, respectively) in Figure 4.

The measurement precision of χ_{BH} is about an order of magnitude better than χ_{NS}. As discussed in Section 2.1, most of the information for χ_{eff} comes from χ_{BH} for highly asymmetric NSBH systems, and χ_{eff} being the best-measured spin parameter

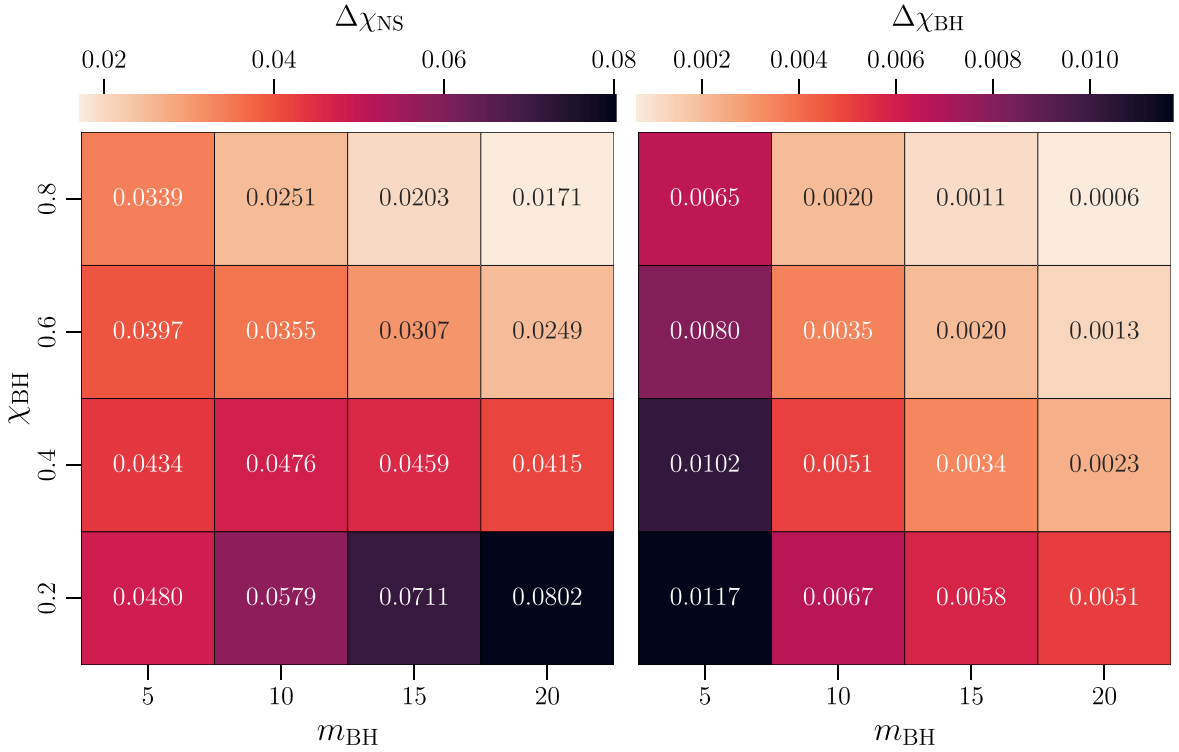

Figure 4. The half-widths of the 68% confidence intervals (i.e., one-sided 1σ widths) corresponding to the bounds on $\chi_{\rm NS}$ (left panel) and $\chi_{\rm BH}$ (right panel) for the 16 NSBH systems with BH mass in $\{5\ M_\odot, 10\ M_\odot, 15\ M_\odot, 20\ M_\odot\}$ and BH spin in $\chi_{\rm BH} \in \{0.2, 0.4, 0.6, 0.8\}$. The NS mass for all the systems was fixed to 1.4 $M_\odot$, the NS spin to 0.04, and ι to 45°.

leads to a precise measurement of $\chi_{\rm BH}$ as well. Further, $\chi_{\rm BH}$ measurement improves both with increasing values of $\chi_{\rm BH}$ and $m_{\rm BH}$, which was anticipated earlier in this section. The behavior of the bounds on $\chi_{\rm NS}$ is more interesting—when $\chi_{\rm BH}$ is small, the bounds on $\chi_{\rm NS}$ worsen with increasing $m_{\rm BH}$, whereas when $\chi_{\rm BH} \gtrsim 0.6$, the bounds on $\chi_{\rm NS}$ improve with higher $m_{\rm BH}$. This is due to two competing effects—as $m_{\rm BH}$ increases, the $\chi_{\rm BH}$ measurement improves (and so the $\chi_{\rm NS}$ measurement should also improve), whereas the contribution of $\chi_{\rm NS}$ to $\chi_{\rm eff}$ and $\tilde{\chi}$ decreases (worsening the measurement of $\chi_{\rm NS}$). It turns out that at low $\chi_{\rm BH}$, the latter effect dominates and $\chi_{\rm NS}$ worsens as $m_{\rm BH}$ increases, whereas at high $\chi_{\rm BH}$, the former effect dominates and $\chi_{\rm NS}$ measurement improves with $m_{\rm BH}$. Stated differently, for high $\chi_{\rm BH}$ values, it is extremely well measured, and it is possible to distinguish between $\chi_{\rm BH}$ and the contribution from $q\,\chi_{\rm NS}$ in $\chi_{\rm eff}$ and $\tilde{\chi}$.

Hence, we see that the $\chi_{\rm NS}$ measurement strongly depends on the values of $\chi_{\rm BH}$. In agreement with our expectations from theoretical arguments, higher $\chi_{\rm BH}$ values are conducive to better $\chi_{\rm NS}$ measurement. For NSBH systems with slowly spinning ($\chi_{\rm BH} < 0.4$) BHs, the bounds on $\chi_{\rm NS}$ worsen with increasing $m_{\rm BH}$, whereas for NSBH systems with highly spinning BHs, higher $m_{\rm BH}$ improves the measurement precision for $\chi_{\rm NS}$.

4.2. Effects of Inclination and HMs

The relative contribution of HMs to the GW waveform increases with inclination angle, which is expected to improve the constraints that can be imposed on $\chi_{\rm NS}$. To evaluate the usefulness of HMs toward $\chi_{\rm NS}$ measurement, we compare the bounds on $\chi_{\rm NS}$ obtained when using a waveform model that contains the dominant (2, ±2) mode as well as HMs to a waveform model that only contains the (2, ±2) mode. For the former, we continue the use of IMRPhenomXHM, and for the latter, we use IMRPhenomXAS (Pratten et al. 2020), which is an aligned-spin waveform model that contains only the quadrupole mode.

We consider the $10+1.4$ NSBH systems with ($\chi_{\rm BH}$, $\chi_{\rm NS}$) = (0.8, 0.04). These are simulated at inclination angles $\iota \in \{0°, 22.°5, 45°, 60°, 90°\}$ and $D_L \in (127, 278)$ Mpc, such that all the systems are detected with the same S/N. The constraints on $\chi_{\rm NS}$ for these systems when injection and parameter estimation are performed with and without HMs are shown in Figure 5. The red plots show the bounds on $\chi_{\rm NS}$ for systems where the waveform contains HMs, whereas the blue plots correspond to those that only contain the quadrupole mode. It is evident from the figure that $\chi_{\rm NS}$ measurement is significantly improved with the increase in the HM contribution to the waveform at greater ι. On the other hand, the constraints on $\chi_{\rm NS}$ for systems where only the quadrupole mode is used are not affected as ι is varied, as the S/N is kept constant. It is also important to note that the $\chi_{\rm NS}$ posteriors of the two sets of injections do not differ considerably until $\iota = 22.°5$. From this, we infer that for such $10+1.4$ systems, HMs are expected to noticeably affect $\chi_{\rm NS}$ measurements only at inclination angles $\iota \gtrsim 45°$. However, GW detections are biased against systems with high ι values; an edge-on system has a similar S/N to a face-on system that is much farther away. Thus, while more GW systems are expected to be oriented face-off, they will be detected with lower S/N compared to face-on systems at the same D_L.

4.3. Effect of Detector Sensitivity

Until now, we have probed the effect of BH properties and HMs on the measurability of $\chi_{\rm NS}$ by keeping the systems at the same S/N (∼700). In this section, we look at the measurability

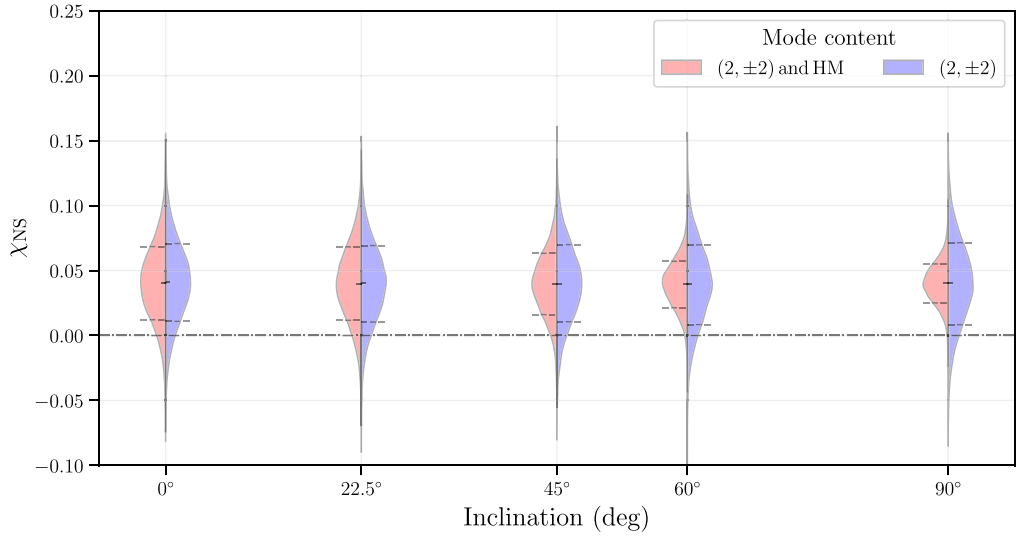

Figure 5. The posterior distributions for the spin of the NS as a function of the inclination angle. The red plots represent the systems for which the injection and the recovery were performed with a waveform that contains both the $(2, \pm 2)$ mode and HMs (IMRPhenomXHM), whereas the blue plots correspond to the systems where the waveform only has the $(2, \pm 2)$ mode (IMRPhenomXAS). The dashed–dotted horizontal line indicates $\chi_{\rm NS} = 0$.

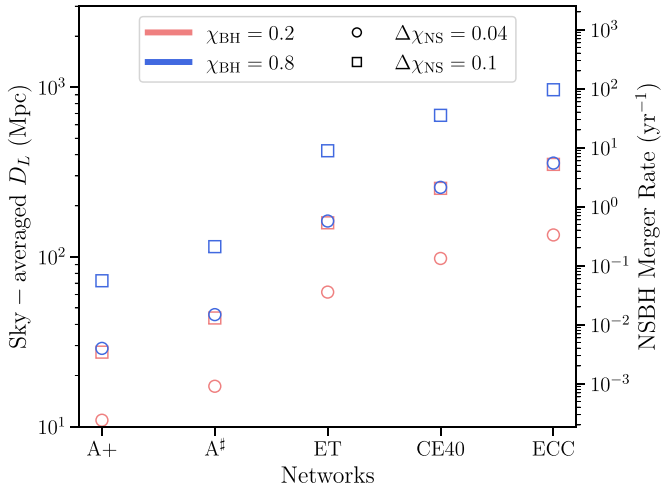

Figure 6. The sky-averaged D_L corresponding to each XG detector network for which a given $\Delta\chi_{\rm NS} \in \{0.04, 0.1\}$ bound can be achieved with a $10 + 1.4$ NSBH system at $\iota = 45°$ and a given $\chi_{\rm BH} \in \{0.2, 0.8\}$. We also denote the corresponding NSBH merger rate per year that is expected at those distances.

as a function of D_L and detector sensitivities. For this purpose, we consider five XG networks: A+ (a network of five detectors at A+ sensitivity), A$^\sharp$ (a network of three detectors with A$^\sharp$ sensitivity), ET (the triangular ET observatory), CE40 (the 40 km CE observatory), and ECC (a network with the triangular ET, the 40 km CE, and the 20 km CE observatories). For a more detailed description of the networks and the different sensitivities, refer to Appendix A. We consider $10 + 1.4$ NSBH systems at $\iota = 45°$. Parameter estimation is performed for two types of systems—first, with a slowly spinning BH ($\chi_{\rm BH} = 0.2$), and second, with a rapidly spinning BH ($\chi_{\rm BH} = 0.8$). In Figure 6, we show the D_L (averaged over the sky) at which the NSBH mergers occur for different XG observatories to obtain (one-sided 1σ) $\Delta\chi_{\rm NS} = 0.04$ and 0.1. Along with the D_L, we also report the corresponding NSBH merger rate up to that distance, which is assumed to follow the Madau–Dickinson star formation rate (Madau & Dickinson 2014; Talbot et al. 2019), and the local merger rate density for NSBH systems is chosen to be $45\,{\rm Gpc^{-3}\,yr^{-1}}$ (Abbott et al. 2021, 2023b; see also Gupta et al. 2023a, 2023b for more details).

For $\chi_{\rm BH} = 0.2$, Figure 6 shows that the chances for A+ or A$^\sharp$ to constrain $\chi_{\rm NS}$ to even $\Delta\chi_{\rm NS} = 0.1$ are bleak, and it would only be possible to do so for a *golden* event that may occur once every 10 to 100 yr. However, networks containing the ET and CE will be able to constrain $\chi_{\rm NS}$ to $\Delta\chi_{\rm NS} = 0.04$ for an event every few years, and $\Delta\chi_{\rm NS} = 0.1$ for a few events every year. For NSBH systems with rapidly spinning BHs, A+ and A$^\sharp$ are expected to constrain $\chi_{\rm NS}$ to $\Delta\chi_{\rm NS} = 0.1$ for events occurring once in 10 yr. Networks with just the ET and/or CE will be able to constrain $\chi_{\rm NS}$ to $\Delta\chi_{\rm NS} = 0.04$ for a few events every year, and to $\Delta\chi_{\rm NS} = 0.1$ for tens of events every year. In fact, the ECC detector can constrain $\chi_{\rm NS}$ to $\Delta\chi_{\rm NS} = 0.1$ for events merging at $\sim$1000 Mpc. Up to this distance, we expect $\sim$100 NSBH mergers every year, which increases the chances of detecting a highly spinning NS.

These estimates will depend on the choice of masses for the system as well as the inclination angle. Both these effects have been explored in the previous sections. Based on the current GW observations, $\chi_{\rm BH}$ in NSBH systems is expected to be low (Biscoveanu et al. 2022). If this is indeed true for the cosmic NSBH population, then resolving the NS spin well enough to differentiate it from 0 may only be possible, realistically, for networks with CE and ET. However, if a rapidly spinning BH were to merge with a rapidly spinning NS, the A+ and A$^\sharp$ networks may constrain $\chi_{\rm NS}$ well enough to distinguish such an NS from a slowly spinning one.

5. Conclusions

GW observations can be used to infer source parameters that can illuminate the astrophysical processes involved in binary formation and evolution. Precise measurements of these parameters, particularly the mass and the spin of the binary components, can be used to distinguish between the different astrophysical formation channels. In this work, we have assessed the measurability of the spins of the NS using NSBH detections with XG GW detector networks.

In Section 2.1, we showed that HMs can contribute significantly to the waveform and the measurement of the NS

spin, especially at higher inclination angles, with (3, ±3) being the second-highest contributor to the $\chi_{\rm NS}$ measurement. We also noted that η interacts with negative combinations of the component spins in the amplitude of the (2, ±1) and the (3, ±3) modes, and with positive combinations of the component spins in the (2, ±2), (3, ±2), and (4, ±4) modes. These different interactions help mitigate the mass–spin degeneracy. However, due to the narrow mass function of the NS, we do not expect an appreciable contribution of HMs to the BNS signal. Hence, we instead look at the bounds that can be placed on $\chi_{\rm NS}$ with NSBH systems, which are naturally mass-asymmetric.

In Section 2.1, we also posit that a higher spin value of the primary will improve the spin measurement of the secondary. This is later confirmed with parameter estimation studies (see Figure 3). In the context of NSBH mergers, this would mean having both the BH and the NS rapidly spinning. In Section 2.2, we discuss the various astrophysical processes, under the constraints of the isolated binary formation channels, that can lead to the formation of such systems. These include compact objects born after core-collapse supernovae that may rapidly rotate due to the stochastic accretion of infalling matter, the spinup of the firstborn compact object by mass accretion due to ultrastripping of the companion Wolf–Rayet star, and an increase in the spin of the secondary due to tidal synchronization with its companion in a close orbit. While the aim of this work is not to justify the existence of such systems, we argue that their detection will provide key insights into the astrophysical processes that govern the formation and evolution of such systems. Thus, in this work, we have assessed the possibility of differentiating a rapidly rotating NS from a slow or nonrotating one, using XG GW observatories.

Using the relative binning technique of accelerated parameter estimation, we performed Bayesian analyses on a set of NSBH systems, the results of which are detailed in Section 4. We find that the constraints on $\chi_{\rm NS}$ are highly contingent on the spin of the companion BH, with high $\chi_{\rm BH}$ values improving the bounds on $\chi_{\rm NS}$ (see Figure 3). We also discussed the effect of $\chi_{\rm BH}$ on the measurement of $\chi_{\rm NS}$ when varying BH mass—for low $\chi_{\rm BH}$ ($\sim$0.2), the bounds on $\chi_{\rm NS}$ get worse as we increase the BH mass, whereas for a rapidly rotating BH ($\chi_{\rm BH} \gtrsim 0.6$), $\chi_{\rm NS}$ is measured better for a more massive BH (see Figure 4).

To show the improvements in $\chi_{\rm NS}$ measurement brought about by HMs, we compare the posterior distribution of $\chi_{\rm NS}$ for $10 + 1.4\ \ M_{\odot}$ NSBH systems for two sets of injections at varying inclination angles—first, with a waveform that contains only the (2, ± 2) mode (IMRPhenomXAS), and second, with a waveform that contains the (2, ± 2) and HMs (IMRPhenomXHM). We find that as the inclination angle increases (and so does the relative HM contribution; see Figure 2), $\chi_{\rm NS}$ measurements improve considerably when HMs are included in the waveform, whereas no significant change is seen in the $\chi_{\rm NS}$ measurement when HMs are not included (see Figure 5), showing the utility of HMs in $\chi_{\rm NS}$ measurement. Finally, we explore the effects of S/N and detector sensitivity on the measurability of $\chi_{\rm NS}$. We find that $\chi_{\rm NS} = 0.1$ can be distinguished from 0 with A+ and A$^\sharp$ for golden events that may occur once in every tens of years. However, if the BH is rapidly rotating ($\chi_{\rm BH} = 0.8$), networks with ET and CE will be able to make the same distinction for $\mathcal{O}(100)$ events, merging up to 1000 Mpc (see Figure 5).

Thus, if a rapidly spinning NS were to merge with a BH, XG observatories with ET and CE would be capable of differentiating such an NS from nonspinning ones, making it the first discovery of such an NS without electromagnetic observations. Such a discovery would be monumental for astrophysical studies on binary formation and evolution. As high values of aligned spins are conducive to the tidal deformation of NSs before merger, such systems can also be important for multimessenger astronomy (Gupta et al. 2023a) and cosmology (Gupta 2023). In this work, we have restricted ourselves to aligned-spin systems. However, with better parameter estimation techniques, this work can be extended to precessing (and even eccentric) NSBH mergers formed due to dynamical interactions. While precession will improve the relative contribution of HM, the additional spin and tilt parameters may increase the uncertainty in $\chi_{\rm NS}$ measurement. Further, the asymmetry between $\pm m$ modes for the precessing system can also play a role in measuring the spins of the components (Kalaghatgi & Hannam 2021; Kolitsidou et al. 2024). Thus, a similar study spanning various binary configurations (in terms of spin and tilt values) will be useful to ascertain if $\chi_{\rm NS}$ can be even better measured than what has been claimed in this work. Another possible extension would be to look at the prospects of detecting a subpopulation of such rapidly spinning NSs with NSBH systems. This may require less stringent bounds on $\chi_{\rm NS}$ for each event, which will increase the number of potential candidates that can contribute to the analysis.

Acknowledgments

I would like to thank Bangalore Sathyaprakash, Debatri Chattopadhyay, and Aditya Vijaykumar for the helpful discussions and important insights, Koustav Chandra for the comments that have helped to improve the manuscript, and Rahul Kashyap, Arnab Dhani, K. G. Arun, Mukesh Kumar Singh, Rossella Gamba, and Sebastiano Bernuzzi for technical suggestions that have been incorporated in this work. This work is funded by the following NSF grants: PHY-2207638, AST-2307147, PHY-2308886, and PHY-2309064.

Appendix A
Detector Configurations

To assess the effect of the detector sensitivity on the measurability of $\chi_{\rm NS}$, we considered five XG detector networks, which are listed in Table 2. The corresponding sensitivities have been plotted in Figure 7.

Table 2
The Detector Configurations Used in Section 4.3

Name	Detectors
A+	Hanford (US), Livingston (US), and Aundha (India) at A+ sensitivity, Virgo (Italy) at V+ sensitivity, and KAGRA (Japan) at K+ sensitivity
A$^\sharp$	Hanford (US), Livingston (US), and Aundha (India) at A$^\sharp$ sensitivity
ET	Triangular ET observatory with three detectors in a xylophone arrangement
CE40	40 km L-shaped CE detector
ECC	Triangular ET, L-shaped 20 km CE, and L-shaped 40 km CE

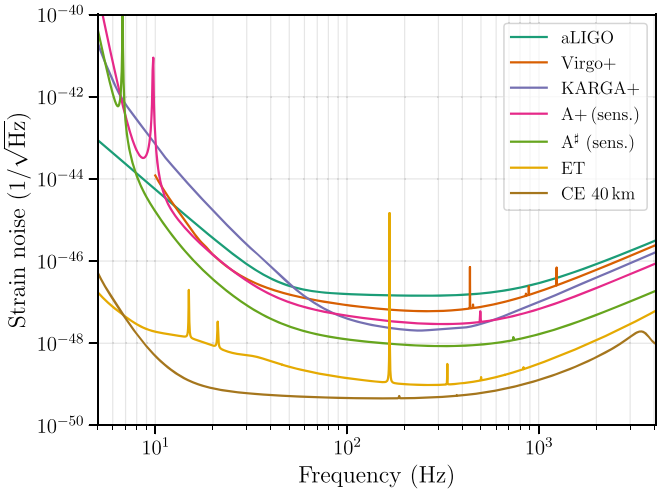

Figure 7. The PSDs for the different sensitivities considered in this work. Here, A+ and A♯ refer to the sensitivity of a given LIGO detector. The files used to generate these curves can be found in the https://gitlab.com/sborhanian/gwbench/-/tree/master/gwbench/noise_curves `gwbench` repository.

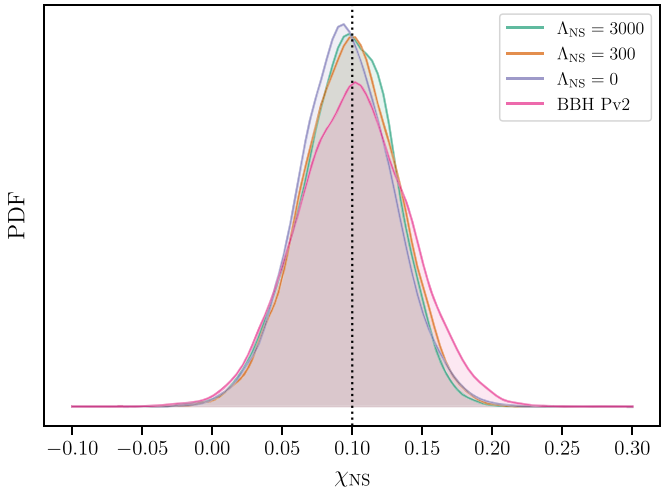

Figure 8. The inferred probability density function for χ_{NS} for NSBH systems with $(m_{BH}, m_{NS}) = (5\ M_\odot, 1.4\ M_\odot)$, at $\iota = 45°$. The dotted vertical line shows the injected value of χ_{NS}.

Appendix B
Effect of Tides on NS Spin Measurement

During NSBH mergers, the NS can get tidally disrupted by the BH. The tidal disruption is affected by the equation of state of the NS, the spins of the components, and the mass ratio of the system (see Kyutoku et al. 2021 for a review). A high χ_{BH} is conducive to the disruption, whereas a higher m_{BH} (hence, a low q) is unfavorable. Most of our estimates have been shown for NSBH systems with $m_{BH} = 10\ M_\odot$ and $m_{NS} = 1.4\ M_\odot$. For this system, even with high BH spins, we do not expect the NS to be significantly disrupted (e.g., Krüger & Foucart 2020). However, for completeness, we show that the tidal contributions, especially through the spin-induced quadrupole moments, will not considerably affect χ_{NS} estimates. To accomplish this, we choose IMRPhenomPv2_NRTidalv2 (Dietrich et al. 2019), which contains the contribution of the tidal terms to the spin-induced quadrupole. Note that a more dedicated NSBH waveform like IMRPhenomNSBH (Thompson et al. 2020) was not used, as it does not allow for spinning NSs. We pair a 5 $M_\odot$ BH (which is the lightest BH considered in this study) with a 1.4 $M_\odot$ NS. The tidal deformability parameter for the BH is assumed to be 0, and for the NS, it is taken to be $\Lambda_{NS} \in \{0, 300, 3000\}$. The (χ_{BH}, χ_{NS}) were chosen to be (0.8, 0.1) to maximize the effect. We also compare these results with BBHs, keeping all parameters the same (except Λ, which would be 0 for a BH) and using the IMRPhenomPv2 (Hannam et al. 2014; Khan et al. 2019) waveform model. Note that while both IMRPhenomPv2 and IMRPhenomPv2_NRTidalv2 allow for precession, we only consider nonprecessing systems in this study. The corresponding plots are shown in Figure 8. From the figure, we do not see a significant difference in the χ_{NS} measurement as the value of Λ_{NS} is increased. The constraints obtained for the BBH waveform model are slightly broader, which may indicate that including spin-induced quadrupole terms helps the χ_{NS} measurement. However, a more detailed study is required to make this assertion. For our purpose, we conclude that including tidal effects will not hamper the χ_{NS} measurement.

ORCID iDs

Ish Gupta https://orcid.org/0000-0001-6932-8715

References

Aasi, J., Abbott, B. P., Abbott, R., et al. 2015, CQGra, 32, 074001
Abbott, B. P., Abbott, R., Abbott, T. D., et al. 2016a, ApJL, 818, L22
Abbott, B. P., Abbott, R., Abbott, T. D., et al. 2016b, PhRvL, 116, 061102
Abbott, B. P., Abbott, R., Abbott, T. D., et al. 2017a, PhRvL, 119, 161101
Abbott, B. P., Abbott, R., Abbott, T. D., et al. 2017b, CQGra, 34, 044001
Abbott, B. P., Abbott, R., Abbott, T. D., et al. 2018, LRR, 21, 3
Abbott, B. P., Abbott, R., Abbott, T. D., et al. 2020a, ApJL, 892, L3
Abbott, B. P., Abbott, R., Abbott, T. D., et al. 2020b, CQGra, 37, 045006
Abbott, R., Abbott, T. D., Abraham, S., et al. 2021, ApJL, 915, L5
Abbott, R., Abbott, T. D., Acernese, F., et al. 2023a, PhRvX, 13, 041039
Abbott, R., Abbott, T. D., Acernese, F., et al. 2023b, PhRvX, 13, 011048
Acernese, F., Agathos, M., Agatsuma, K., et al. 2015, CQGra, 32, 024001
Acernese, F., Agathos, M., Aiello, L., et al. 2019, PhRvL, 123, 231108
Ajith, P., Hannam, M., Husa, S., et al. 2011, PhRvL, 106, 241101
Alsing, J., Silva, H. O., & Berti, E. 2018, MNRAS, 478, 1377
Antoniadis, J., Tauris, T. M., Ozel, F., et al. 2016, arXiv:1605.01665
Arun, K. G., Buonanno, A., Faye, G., & Ochsner, E. 2009, PhRvD, 79, 104023
Ashton, G., Hübner, M., Lasky, P. D., et al. 2019, ApJS, 241, 27
Baird, E., Fairhurst, S., Hannam, M., & Murphy, P. 2013, PhRvD, 87, 024035
Bavera, S. S., Fragos, T., Zevin, M., et al. 2021, A&A, 647, A153
Belczynski, K., Holz, D. E., Bulik, T., & O'Shaughnessy, R. 2016, Natur, 534, 512
Belczynski, K., Kalogera, V., Rasio, F. A., Taam, R. E., & Bulik, T. 2007, ApJ, 662, 504
Benacquista, M. J., & Downing, J. M. B. 2013, LRR, 16, 4
Berti, E., & Volonteri, M. 2008, ApJ, 684, 822
Biscoveanu, S., Landry, P., & Vitale, S. 2022, MNRAS, 518, 5298
Blanchet, L. 2014, LRR, 17, 2
Borhanian, S. 2021, CQGra, 38, 175014
Branchesi, M., Maggiore, M., Alonso, D., et al. 2023, JCAP, 07, 068
Broekgaarden, F. S., Berger, E., Neijssel, C. J., et al. 2021, MNRAS, 508, 5028
Buchner, J., Georgakakis, A., Nandra, K., et al. 2014, A&A, 564, A125
Buikema, A., Cahillane, C., Mansell, G. L., et al. 2020, PhRvD, 102, 062003
Burgay, M., D'Amico, N., Possenti, A., et al. 2003, Natur, 426, 531
Burrows, A., Vartanyan, D., & Wang, T. 2023a, ApJ, 957, 68
Burrows, A., Wang, T., Vartanyan, D., & Coleman, M. S. B. 2023b, arXiv:2311.12109
Canizares, P., Field, S. E., Gair, J., et al. 2015, PhRvL, 114, 071104
Cantiello, M., Mankovich, C., Bildsten, L., Christensen-Dalsgaard, J., & Paxton, B. 2014, ApJ, 788, 93
Chattopadhyay, D., Stevenson, S., Broekgaarden, F., Antonini, F., & Belczynski, K. 2022, MNRAS, 513, 5780
Chattopadhyay, D., Stevenson, S., Hurley, J. R., Bailes, M., & Broekgaarden, F. 2021, MNRAS, 504, 3682

Chatziioannou, K., Cornish, N., Klein, A., & Yunes, N. 2014, PhRvD, 89, 104023
Coleman, M. S. B., & Burrows, A. 2022, MNRAS, 517, 3938
Cornish, N. J. 2010, arXiv:1007.4820
Cornish, N. J. 2021, PhRvD, 104, 104054
Cutler, C., & Flanagan, E. E. 1994, PhRvD, 49, 2658
Delgado, A. J., & Thomas, H. C. 1981, A&A, 96, 142
Dhani, A., Völkel, S., Buonanno, A., et al. 2024, arXiv:2404.05811
Dietrich, T., Samajdar, A., Khan, S., et al. 2019, PhRvD, 100, 044003
Doroshenko, V., Suleimanov, V., Pühlhofer, G., & Santangelo, A. 2022, NatAs, 6, 1444
Edwards, T. D. P., Wong, K. W. K., Lam, K. K. H., et al. 2023, arXiv:2302.05329
Evans, M., Adhikari, R. X., Afle, C., et al. 2021, arXiv:2109.09882
Evans, M., Corsi, A., Afle, C., et al. 2023, arXiv:2306.13745
Farah, A. M., Edelman, B., Zevin, M., et al. 2023, ApJ, 955, 107
Farr, B., Holz, D. E., & Farr, W. M. 2018, ApJL, 854, L9
Farr, W. M., & Chatziioannou, K. 2020, RNAAS, 4, 65
Farr, W. M., Sravan, N., Cantrell, A., et al. 2011, ApJ, 741, 103
Farr, W. M., Stevenson, S., Coleman Miller, M., et al. 2017, Natur, 548, 426
Fritschel, P., Kuns, K., Driggers, J., et al. 2022, Prospects for doubling the range of Advanced LIGO T2200287, LIGO, https://dcc.ligo.org/LIGO-T2200287/public
Fuller, J., & Lu, W. 2022, MNRAS, 511, 3951
Fuller, J., & Ma, L. 2019, ApJL, 881, L1
García-Quirós, C., Colleoni, M., Husa, S., et al. 2020, PhRvD, 102, 064002
Ge, H., Hjellming, M. S., Webbink, R. F., Chen, X., & Han, Z. 2010, ApJ, 717, 724
Ge, H., Webbink, R. F., Chen, X., & Han, Z. 2015, ApJ, 812, 40
Gerosa, D., & Berti, E. 2017, PhRvD, 95, 124046
Green, S. R., Simpson, C., & Gair, J. 2020, PhRvD, 102, 104057
Gupta, I. 2023, MNRAS, 524, 3537
Gupta, I., Borhanian, S., Dhani, A., et al. 2023a, PhRvD, 107, 124007
Gupta, I., Afle, C., Arun, K. G., et al. 2023b, arXiv:2307.10421
Hannam, M., Schmidt, P., Bohé, A., et al. 2014, PhRvL, 113, 151101
Hastings, W. K. 1970, Bimka, 57, 97
Hessels, J. W. T., Ransom, S. M., Stairs, I. H., et al. 2006, Sci, 311, 1901
Hild, S., Abernathy, M., Acernese, F., et al. 2011, CQGra, 28, 094013
Hu, Q., & Veitch, J. 2022, PhRvD, 106, 044042
Hu, R.-C., Zu, J.-P., Qin, Y., et al. 2023, arXiv:2301.06402
Huang, Y., Chen, H.-Y., Haster, C.-J., et al. 2022, arXiv:2204.03614
Janquart, J., Baka, T., Samajdar, A., Dietrich, T., & Van Den Broeck, C. 2023, MNRAS, 523, 1699
Johnson, A. D., Chatziioannou, K., & Farr, W. M. 2024, PhRvD, 109, 084015
Kalaghatgi, C., & Hannam, M. 2021, PhRvD, 103, 024024
Kalogera, V. 2000, ApJ, 541, 319
Khan, S., Chatziioannou, K., Hannam, M., & Ohme, F. 2019, PhRvD, 100, 024059
Kiziltan, B., Kottas, A., De Yoreo, M., & Thorsett, S. E. 2013, ApJ, 778, 66
Kolitsidou, P., Thompson, J. E., & Hannam, M. 2024, arXiv:2402.00813
Koposov, S., Speagle, J., Barbary, K., et al. 2023, joshspeagle/dynesty: v2.1.3, v2.1.3, Zenodo, doi:10.5281/zenodo.8408702
Krishna, K., Vijaykumar, A., Ganguly, A., et al. 2023, arXiv:2312.06009
Krishnendu, N. V., Arun, K. G., & Mishra, C. K. 2017, PhRvL, 119, 091101
Krüger, C. J., & Foucart, F. 2020, PhRvD, 101, 103002
Kushnir, D., Zaldarriaga, M., Kollmeier, J. A., & Waldman, R. 2017, MNRAS, 467, 2146
Kyutoku, K., Shibata, M., & Taniguchi, K. 2021, LRR, 24, 5
Landry, P., & Read, J. S. 2021, ApJL, 921, L25
Leslie, N., Dai, L., & Pratten, G. 2021, PhRvD, 104, 123030
Lorimer, D. R. 2008, LRR, 11, 8
Madau, P., & Dickinson, M. 2014, ARA&A, 52, 415
Mandel, I., & Farmer, A. 2022, PhR, 955, 1
Margalit, B., & Metzger, B. D. 2017, ApJL, 850, L19
Mastrogiovanni, S., Lamberts, A., Srinivasan, R., Bruel, T., & Christensen, N. 2022, MNRAS, 517, 3432
Mennekens, N., & Vanbeveren, D. 2014, A&A, 564, A134
Metropolis, N., Rosenbluth, A. W., Rosenbluth, M. N., Teller, A. H., & Teller, E. 1953, JChPh, 21, 1087
Miller, J., Barsotti, L., Vitale, S., et al. 2015, PhRvD, 91, 062005
Mills, C., & Fairhurst, S. 2021, PhRvD, 103, 024042
Morisaki, S. 2021, PhRvD, 104, 044062
Morisaki, S., & Raymond, V. 2020, PhRvD, 102, 104020
Morisaki, S., Smith, R., Tsukada, L., et al. 2023, PhRvD, 108, 123040
Nagar, A., Bernuzzi, S., Pozzo, W. D., et al. 2018, PhRvD, 98, 104052
Olejak, A., & Belczynski, K. 2021, ApJL, 921, L2
O'Shaughnessy, R., Gerosa, D., & Wysocki, D. 2017, PhRvL, 119, 011101
Ozel, F., Psaltis, D., Narayan, R., & Villarreal, A. S. 2012, ApJ, 757, 55
Pan, Y., Buonanno, A., Fujita, R., Racine, E., & Tagoshi, H. 2011, PhRvD, 83, 064003
Pankow, C., Brady, P., Ochsner, E., & O'Shaughnessy, R. 2015, PhRvD, 92, 023002
Pathak, L., Munishwar, S., Reza, A., & Sengupta, A. S. 2024, PhRvD, 109, 024053
Pathak, L., Reza, A., & Sengupta, A. S. 2023, PhRvD, 108, 064055
Postnov, K. A., & Yungelson, L. R. 2014, LRR, 17, 3
Pratten, G., Husa, S., Garcia-Quiros, C., et al. 2020, PhRvD, 102, 064001
Punturo, M., Abernathy, M., Acernese, F., et al. 2010, CQGra, 27, 194002
Pürrer, M., & Haster, C.-J. 2020, PhRvR, 2, 023151
Qin, Y., Fragos, T., Meynet, G., et al. 2018, A&A, 616, A28
Reitze, D., Adhikari, R. X., Ballmer, S., et al. 2019, BAAS, 51, 035
Rezzolla, L., Most, E. R., & Weih, L. R. 2018, ApJL, 852, L25
Rodriguez, C. L., Zevin, M., Pankow, C., Kalogera, V., & Rasio, F. A. 2016, ApJL, 832, L2
Romero-Shaw, I. M., Talbot, C., Biscoveanu, S., et al. 2020, MNRAS, 499, 3295
Roy, S., Sengupta, A. S., & Arun, K. G. 2021, PhRvD, 103, 064012
Ruiz, M., Shapiro, S. L., & Tsokaros, A. 2018, PhRvD, 97, 021501
Samajdar, A., Janquart, J., Van Den Broeck, C., & Dietrich, T. 2021, PhRvD, 104, 044003
Shibata, M., Fujibayashi, S., Hotokezaka, K., et al. 2017, PhRvD, 96, 123012
Shibata, M., Zhou, E., Kiuchi, K., & Fujibayashi, S. 2019, PhRvD, 100, 023015
Sigurdsson, S., & Hernquist, L. 1993, Natur, 364, 423
Skilling, J. 2004, in AIP Conf. Proc. 735, 24th Int. Workshop on Bayesian Inference and Maximum Entropy Methods in Science and Engineering (Melville, NY: AIP), 395
Smith, R., Field, S. E., Blackburn, K., et al. 2016, PhRvD, 94, 044031
Smith, R. J. E., Ashton, G., Vajpeyi, A., & Talbot, C. 2020, MNRAS, 498, 4492
Soberman, G. E., Phinney, E. S., & den Heuvel, E. P. J. V. 1997, A&A, 327, 620
Speagle, J. S. 2020, MNRAS, 493, 3132
Sun, L., Goetz, E., Kissel, J. S., et al. 2020, CQGra, 37, 225008
Sun, L., Goetz, E., Kissel, J. S., et al. 2021, arXiv:2107.00129
Suwa, Y., Yoshida, T., Shibata, M., Umeda, H., & Takahashi, K. 2018, MNRAS, 481, 3305
Talbot, C., Smith, R., Thrane, E., & Poole, G. B. 2019, PhRvD, 100, 043030
Tauris, T. M., Langer, N., & Podsiadlowski, P. 2015, MNRAS, 451, 2123
Thompson, J. E., Fauchon-Jones, E., Khan, S., et al. 2020, PhRvD, 101, 124059
Thorne, K. S. 1974, ApJ, 191, 507
Thrane, E., & Talbot, C. 2019, PASA, 36, e010
Tiwari, V. 2022, ApJ, 928, 155
Tiwari, V., & Fairhurst, S. 2021, ApJL, 913, L19
Tiwari, V., Hoy, C., Fairhurst, S., & MacLeod, D. 2023, PhRvD, 108, 023001
Tse, M., Yu, H., Kijbunchoo, N., et al. 2019, PhRvL, 123, 231107
Tutukov, A., & Yungelson, L. 1973, NInfo, 27, 70
Tutukov, A. V., & YungelSon, L. R. 1993, MNRAS, 260, 675
Vigna-Gómez, A., Neijssel, C. J., Stevenson, S., et al. 2018, MNRAS, 481, 4009
Vinciguerra, S., Veitch, J., & Mandel, I. 2017, CQGra, 34, 115006
Vitale, S., Biscoveanu, S., & Talbot, C. 2022, A&A, 668, L2
Vitale, S., Lynch, R., Sturani, R., & Graff, P. 2017, CQGra, 34, 03LT01
Wang, Z.-H.-T., Hu, R.-C., Qin, Y., et al. 2024, ApJ, 965, 177
Williams, M. J. 2021, nessai: Nested Sampling with Artificial Intelligence, v0.12.0, Zenodo, doi:10.5281/zenodo.4550693
Williams, M. J., Veitch, J., & Messenger, C. 2021, PhRvD, 103, 103006
Williams, M. J., Veitch, J., & Messenger, C. 2023, MLS&T, 4, 035011
Wong, K. W. K., Breivik, K., Kremer, K., & Callister, T. 2021, PhRvD, 103, 083021
Wong, K. W. K., Isi, M., & Edwards, T. D. P. 2023, ApJ, 958, 129
Wu, S., & Nitz, A. H. 2023, PhRvD, 107, 063022
Zackay, B., Dai, L., & Venumadhav, T. 2018, arXiv:1806.08792
Zaldarriaga, M., Kushnir, D., & Kollmeier, J. A. 2018, MNRAS, 473, 4174
Zevin, M., & Bavera, S. S. 2022, ApJ, 933, 86
Zevin, M., Bavera, S. S., Berry, C. P. L., et al. 2021, ApJ, 910, 152
Zevin, M., Pankow, C., Rodriguez, C. L., et al. 2017, ApJ, 846, 82
Zhang, C. M., & Kojima, Y. 2006, MNRAS, 366, 137